analytical chemistry

pubs.acs.org/ac Article

Dual-Engine Powered Paper Photoelectrochemical Platform Based on 3D DNA Nanomachine-Mediated CRISPR/Cas12a for Detection of Multiple miRNAs

Chuan Huang,[⊥] Lu Zhang,[⊥] Yuanna Zhu, Zuhao Zhang, Yunqing Liu, Chao Liu,* Shenguang Ge,* and Jinghua Yu

Cite This: *Anal. Chem.* 2022, 94, 8075−8084 Read Online

ACCESS | Metrics & More | Article Recommendations | Supporting Information

ABSTRACT: This work proposed a novel double-engine powered paper photoelectrochemical (PEC) biosensor based on an anode−cathode cooperative amplification strategy and various signal enhancement mechanisms, which realized the monitoring of multiple miRNAs (such as miRNA-141 and miRNA-21). Specifically, C_3N_4 quantum dots (QDs) sensitized ZnO nanostars and BiOI nanospheres simultaneously to construct a composite photoelectric layer that amplified the original photocurrent of the photoanode and photocathode, respectively. Through the independent design and partition of a flexible paper chip to functionalize injection holes and electrode areas, the bipolar combination completed the secondary upgrade of signals, which also provided biological reaction sites for multitarget detection. With the synergistic participation of a three-dimensional (3D) DNA nanomachine and programmable CRISPR/Cas12a shearing tool, C_3N_4 QDs lost their attachment away from the electrode surface to quench the signal. Moreover, electrode zoning significantly reduced the spatial cross talk of related substances for multitarget detection, while the universal trans-cleavage capability of CRISPR/Cas12a simplified the operation. The designed PEC biosensor revealed excellent linear ranges for detection of miRNA-141 and miRNA-21, for which the detection limits were 5.5 and 3.4 fM, respectively. With prominent selectivity and sensitivity, the platform established an effective approach for trace multitarget monitoring in clinical applications, and its numerous pioneering attempts owned favorable reference values.

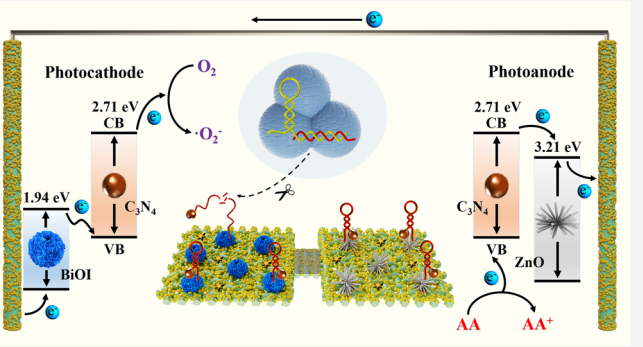

INTRODUCTION

MicroRNAs (miRNAs) are a crucial regulator of gene expression and play a pivotal role in pathogenesis and treatment of various malignant diseases.[1,2] In particular, the literature has proved that any microRNA is not isolated but tends to cooperatively participate in the whole development process of the disease.[3] Therefore, the accurate detection of miRNA (especially, multiple miRNAs) content possesses a guiding significance for disease prevention and diagnosis. Among the mainstream analytical equipment, photoelectrochemical (PEC) biosensors stand out because of their simple operation, high sensitivity, and wide applicability.[4,5]

PEC biosensors are generally classified into photoanode biosensors and photocathode biosensors according to different signal output forms. Photoanode biosensors with an ideal photocurrent intensity depend on electron-rich n-type semiconductors (TiO_2,[6] WO_3[7] and $AgInS_2$[8]), while photocathode biosensors against the interference of reducing substances are based on hole-abundant p-type semiconductors (Cu_2O,[9] $CuInS_2$,[10] and PbS[11]). With the basis of photoelectric conversion, the development and utilization of semiconductor materials are deepening.[12] With a widely concerned n-type semiconductor, ZnO nanostars (NSs) own a larger active surface area and higher carrier separation efficiency than the conventional morphology,[13,14] which are expected to be applied in the field of photoelectrochemistry. For p-type semiconductors, BiOI nanospheres have attracted much attention due to their novel layered rough structure and effective narrow band gap,[15,16] meaning extremely efficient acquisition of visible light. Although the above materials have significant advantages, they also have limitations such as a broad band gap of ZnO NSs and a high electron−hole recombination rate of BiOI nanospheres. To overcome the constraints of pure PEC materials, energy-level-matched

Received: April 19, 2022
Accepted: May 13, 2022
Published: May 24, 2022

https://doi.org/10.1021/acs.analchem.2c01717
Anal. Chem. 2022, 94, 8075−8084

Scheme 1. (A) Target Conversion and Amplification Mechanism of the 3D DNA Nanomachine and Activation Principle of CRISPR/Cas12a. (B) Schematic Diagram of the Dual-Engine PEC Biosensor Based on the trans-Cleavage Activity of CRISPR/Cas12a

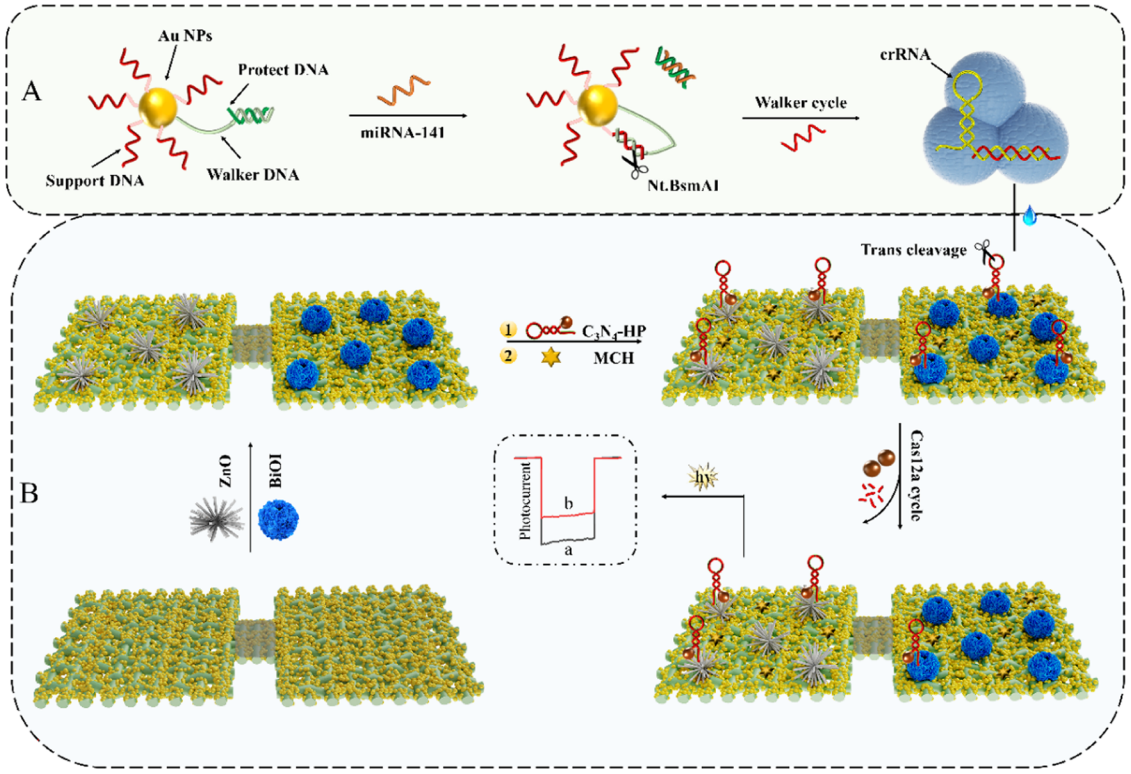

semiconductors are often selected to sensitize substrate semiconductors, such as a series of quantum dots (QDs).[17,18] In recent years, C_3N_4 QDs with an appropriate energy level and excellent photostability have been widely reported in the area of photocatalysis,[19,20] but their potential as PEC materials needs to be developed.

The traditional photoanode/photocathode biosensors based on the three-electrode mode have problems related to spatial interference, such as contact cross talk between electrodes and interference of electrolytes on electron transfer both caused by co-region detection.[21,22] On the one hand, the photoanode and photocathode are employed simultaneously to replace the original single photoelectrode, so that the dual power of mutual excitation is obtained to amplify the photocurrent signal.[23] On the other hand, owing to the flexibility and biocompatibility of a paper-based microfluidic chip,[24,25] spatial segmentation is realized between electrodes to increase physical spacing and reduce interference. More importantly, through the independent design and division of a paper chip, the number of sample injection holes and electrode reaction zones can be freely controlled, so as to realize the detection of two or more targets on one device. Therefore, a dual-engine powered paper-based microfluidic model with a photoanode and photocathode owning multicomponent detection ability is constructed for the first time.

Although the proposed platform is interesting and significant, it is still necessary to combine appropriate nucleic acid amplification and sensing recognition strategies to complete the sensitive detection of ultralow content miRNAs in biological samples. As a novel amplification method, the DNA nanomachine integrates specificity, predictability, and efficiency,[26,27] which realizes directional transmission and continuous accumulation of signals through DNA conformational changes stimulated by external targets. Furthermore, the three-dimensional (3D) DNA nanomachine extends the original operation plane to a higher level and exhibits excellent mobility, carrying capacity, and target cycle efficiency, thus achieving extraordinary success in the field of analysis.[28,29] A sensing recognition strategy, a crucial part of the biosensor, causes signal enhancement or quenching through a unique mechanism (mostly various enzymatic reactions). Recently, a clustered regularly interspaced short palindromic repeat (CRISPR)-associated protein (Cas) system is revolutionizing aspects related to gene editing and medical diagnosis, including biosensors.[30,31] Among the CRISPR-Cas family, CRISPR/Cas12a (LbCpf1), a protease that bonds to single-strand DNA (ssDNA) directed CRISPR RNA (crRNA), can not only perform specific cleavage (cis-cleavage) near the 22nd base of the target ssDNA without relying on the protospacer adjacent motif region but also randomly cleave any ssDNA (trans-cleavage) outside the ternary complex system.[32] The universal trans-cleavage characteristic greatly simplifies the operation difficulty and significantly improves the detection sensitivity, which has been widely developed in fluorescent biosensors[33,34] but a lack of research in PEC biosensors.

Combining the advantages of materials, devices, and sensing strategies, a dual-engine powered paper microfluidic biosensor based on a 3D DNA nanomachine-mediated CRISPR/Cas12a system is proposed for detection of multiple miRNAs, such as miRNA-141 and miRNA-21. Taking the monitoring of miRNA-141 as an example, the specific construction process and reaction mechanism are as follows. Scheme 1A shows that superconducting Au nanoparticles (NPs) initially anchored walker DNA (locked by protect DNA) and support DNA

https://doi.org/10.1021/acs.analchem.2c01717
Anal. Chem. 2022, 94, 8075−8084

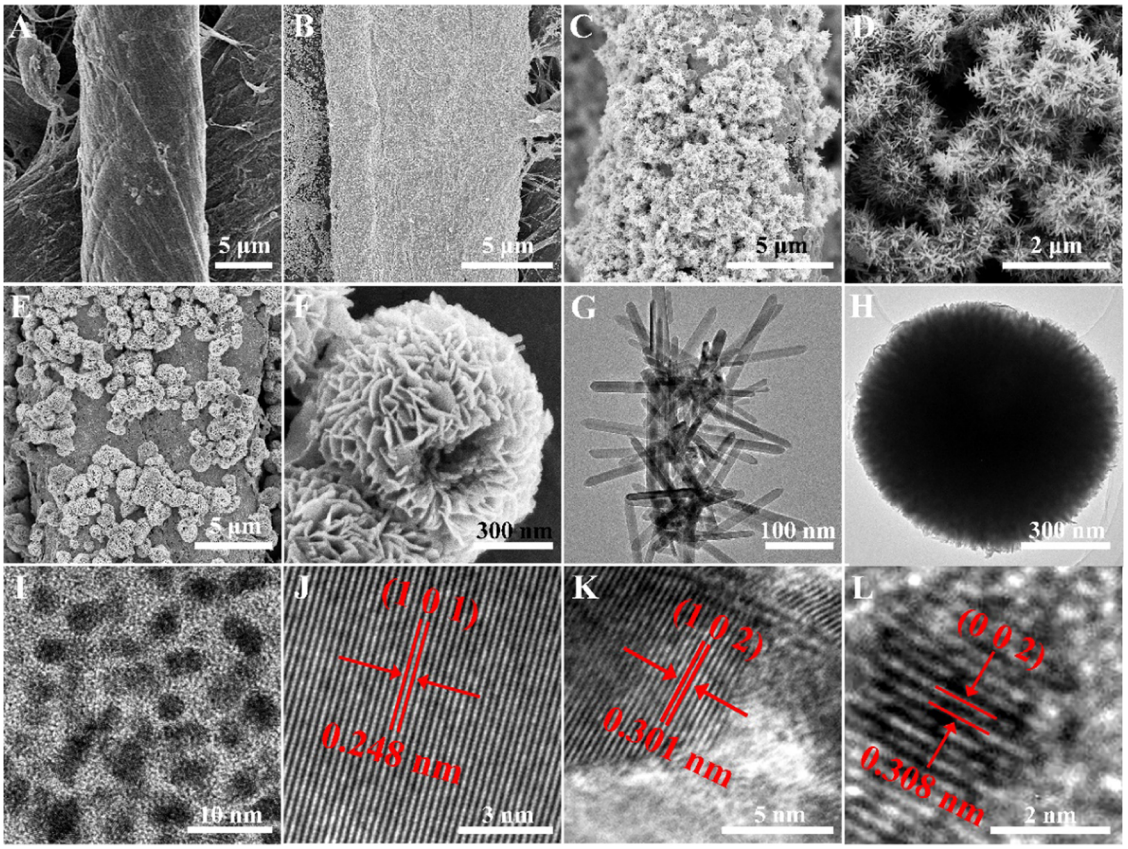

Figure 1. SEM image of (A) bare PWE, (B) Au-PWE, (C) ZnO NSs/Au-PWE, (D) ZnO NSs with high magnification, (E) BiOI nanospheres/Au-PWE, and (F) individual BiOI nanosphere. TEM image of (G) ZnO NSs, (H) BiOI nanospheres, and (I) C_3N_4 QDs. HRTEM image of (J) ZnO NSs, (K) BiOI nanospheres, and (L) C_3N_4 QDs.

through Au−S bond coordination to establish the 3D DNA nanomachine. Subsequently, the introduced target miRNA-141 was entirely complementary to the protect DNA to release walker DNA, while the free walker DNA tended to hybridize with the support DNA and expose the cleavage site of the Nt.*Bsm*AI endonuclease. The required ssDNA continued to accumulate with alternating digestion and DNA walker processes and ultimately participated in the activation of the nonspecific trans-cleavage ability of CRISPR/Cas12a. Scheme 1B displays the assembly process of a dual-target PEC biosensor. First, Au nanomaterials were loaded on the electrode in situ to improve the conductivity and specific surface area, while a secondary batik was performed in the electrode connection to construct the hydrophobic conductive layer for realizing the spatial division between the electrodes. Then, ZnO NSs and BiOI nanospheres were immobilized on the surface of a Au paper working electrode (Au-PWE) to form a photoelectric substrate layer. Immediately, the C_3N_4 QD-anchored hairpin DNA (C_3N_4-HP) was introduced to fabricate a photoelectric sensitization layer by the acylation reaction, which realized the cascade amplification of the initial photoelectric signal. After blocking active sites with 6-mercapto-1-hexanol (MCH), the activated reaction solution obtained in Scheme 1A was dropped from the injection hole into the cathode area of the prepared biosensor. With the random cutting characteristics of CRISPR/Cas12a, the hairpin DNA was cleaved, resulting in the separation of C_3N_4 QDs from the base photoelectric layer to destroy the originally matched energy band combination, and finally reacted to the quenching of photocurrent signals. Similarly, the detection of target miRNA-21 only needed to inject the conversion reaction solution into the anode region.

EXPERIMENTAL SECTION

Materials and Apparatus. The materials and apparatus are shown in the Supporting Information.

Synthesis of ZnO NSs and BiOI Nanospheres. Amino-functionalization of ZnO NSs and BiOI nanospheres was synthesized by the chemical bath deposition and solvothermal methods, respectively, on the basis of previous works (complete steps are described in the Supporting Information).[13,15]

Preparation of Transformational DNA. The preparation and amplification of transformational DNA were achieved by the 3D DNA nanomachine, as detailed below. First, the carrier Au NPs were synthesized by appropriately ameliorating the traditional preparation approach.[35] Meanwhile, 10 μL of walker DNA (1 μM) and 10 μL of protect DNA (1 μM) were dissolved in 80 μL of buffer and annealed at 95 °C for 5 min to form the dsDNA. After that, the above procured 20 μL of Au NPs, 10 μL of dsDNA, and 10 μL of support DNA (2 μM) were mixed in 60 μL of phosphate-buffered solution (PBS) and stirred overnight to establish the 3D DNA nanomachine. Then, 10 μL of different concentrations of target miRNA-141 or miRNA-21 was added and spontaneously paired with protect DNA at 37 °C for 2 h, thereby releasing walker DNA. Consequently, the unlocked walker DNA tended to hybridize with the corresponding support

https://doi.org/10.1021/acs.analchem.2c01717
Anal. Chem. 2022, 94, 8075−8084

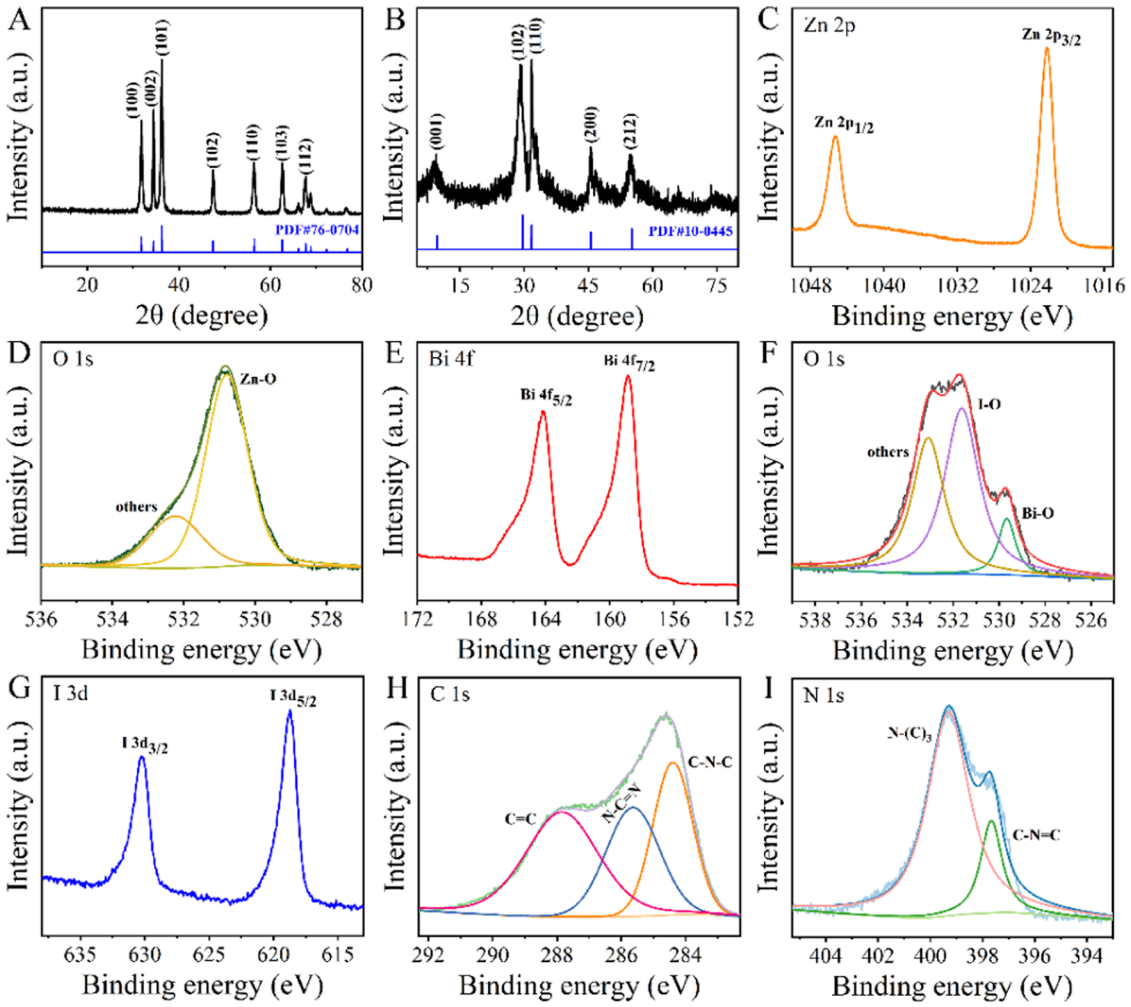

Figure 2. XRD pattern of (A) ZnO NSs and (B) BiOI nanospheres. High-resolution XPS spectra of (C) Zn 2p and (D) O 1s in ZnO NSs. High-resolution XPS spectra of (E) Bi 4f, (F) O 1s, and (G) I 3d in BiOI nanospheres. High-resolution XPS spectra of (H) C 1s and (I) N 1s in C_3N_4 QDs.

DNA into a double helix structure, exposing the recognition site of endonuclease Nt.*Bsm*AI. Ultimately, after 5 U/mL Nt.*Bsm*AI cleaved at 37 °C for 2 h, the required DNA fragment was acquired and walker DNA was released again. The walker DNA continuously migrated and circulated along the surface of Au NPs to achieve a large accumulation of transformational DNA (T-DNA). The required T-DNA was obtained by centrifugation, and the control experiment was performed to further prove that the support DNA anchored on Au NPs did not participate in the subsequent CRISPR/Cas12a activation process to eliminate the interference of false-positive signals (Figure S1).

Construction of a CRISPR/Cas12a-Participated Dual-Target PEC Biosensor. First, according to the paper chip pattern designed by Adobe Illustrator CS4 software, the preliminary batik was implemented through a wax printer to construct multiple injection holes and corresponding electrode areas (Figure S2A). Subsequently, the Ag/AgCl reference electrode was introduced by screen printing, and Au NPs were grown in situ on both sides of the anode−cathode region to improve the electrode conductivity (Figure S2B,C). It was worth mentioning that a secondary batik was performed at the junction of the anode and cathode to functionalize the waterproof electronic bridge, which increased the physical spacing to reduce the interference between the electrodes. Finally, the surface of the electrode area was washed with ultrapure water to remove the floating color. Figure S3 shows the real model of the paper chip device. The controllable output of the anode or cathode photocurrent could be realized by simply exchanging the electrode clip, so as to meet the requirement of dual-target detection. In addition, Figure S4 displays the conceptual diagram of a paper chip with multitarget monitoring capability to expand the analysis potential.

The paper chip was further modified to construct the biosensor. First, 5 mg/mL aminated ZnO and BiOI were loaded as a photoanode and photocathode, respectively, through spin-coating technology. After that, 20 μL of C_3N_4-HP (preparation details in the Supporting Information) treated with EDC and NHS was incubated on the substrate photoelectrode at 4 °C for 6 h. Then, 20 μL of MCH was added to the modified electrode and maintained for 1 h to block active sites. Finally, 20 μL of the mixture consisting of 120 nM crRNA, 100 nM Cas12a, 1× reaction buffer, and as-obtained T-DNA was incubated on the revised electrode at 25 °C for 1 h. Once the Cas12a/crRNA/T-DNA ternary complex was formed, the complex showed strong nonspecific trans-cleavage activity and digested hairpin DNA (HP) into

https://doi.org/10.1021/acs.analchem.2c01717
Anal. Chem. 2022, 94, 8075−8084

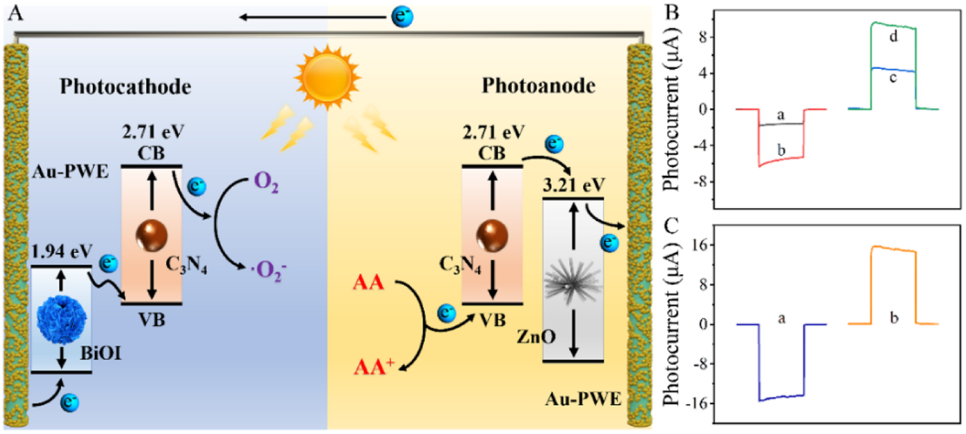

Figure 3. (A) Mechanism of the anode−cathode cooperative enhancement strategy. (B) Photocurrent response to verify the sensitization of C_3N_4: (a) BiOI photocathode with a blank photoanode, (b) C_3N_4/BiOI photocathode with a blank photoanode, (c) ZnO photoanode with a blank photocathode, and (d) C_3N_4/ZnO photoanode with a blank photocathode. (C) Photocurrent response of anode−cathode integration: (a) C_3N_4/BiOI photocathode with a C_3N_4/ZnO photoanode and (b) C_3N_4/ZnO photoanode with a C_3N_4/BiOI photocathode.

fragments. Notably, the surface of the paper electrode was rinsed with buffer after each incubation step to remove the residue. Under the irradiation of a xenon lamp, the photoanode area adopted 0.1 M PBS (containing 0.1 M ascorbic acid, pH 7.4), while the photocathode area selected 0.1 M Tris-HCl (oxygenated, pH 7.4) without voltage for PEC measurements.

RESULTS AND DISCUSSION

Characterization of Materials. The morphology of the prepared electrode and materials was preliminarily characterized by a scanning electron microscope (SEM). Figure 1A shows that the unmodified bare electrode consisted of crisscross rough paper fibers. After introducing Au NPs on the surface of the paper electrode to improve its conductivity, a layer of uniform granular load appeared on the fiber surface in Figure 1B, proving the successful construction of Au-PWE. Photoelectric materials were further modified on Au-PWE to build the photoanode and photocathode. As displayed in Figure 1C, dense ZnO was coated on the electrode surface, which greatly increased the specific surface area and daylighting ability. The high magnification SEM image of ZnO in Figure 1D showed that they were formed by spatial stacking of nanorods with a star-like and unified morphology. Figure 1E shows that when three-dimensional BiOI nanospheres were functionalized on the electrode surface, they were tightly distributed along the radial direction to further improve the roughness of the fiber. Figure 1F obviously exhibits that the BiOI nanospheres were assembled by layered nanosheets, and the hollow configuration might provide an orbit for electrons to speed up the transfer rate.

The size and crystal appearance of ZnO NSs, BiOI nanospheres, and C_3N_4 QDs were fully explored by transmission electron microscopy (TEM) and high-resolution transmission electron microscopy (HRTEM). Figure 1G shows that the overall diameter of the synthesized ZnO was about 350 nm, and the star cluster was stacked from inside to outside by cone-headed nanorods with a width of 20 nm. Figure 1H reveals that the diameter of BiOI similar to ellipsoid was around 1 μm, and the outer edge was relatively loose and rough. Figure 1I showed that C_3N_4 with a diameter ranging from 3 to 5 nm was approximately circular. Moreover, Figure 1J−L represents HRTEM images of ZnO, BiOI, and C_3N_4 separately. Distinct and straight lattice stripes indicated that the prepared materials owned excellent crystallinity, and the lattice spacing corresponded to their respective crystal planes.

The crystal structure and elemental composition of ZnO NSs, BiOI nanospheres, and C_3N_4 QDs were analyzed by X-ray diffraction (XRD) and X-ray photoelectron spectroscopy (XPS). As shown in Figure 2A, any sharp peak of ZnO highly corresponded to the standard PDF card (No. 76-0704), belonging to the typical hexagonal phase.[36] The diffraction peaks of the tetragonal BiOI crystal were consistent with JCPDS No. 10-0445,[37] which was the effective evidence for its successful synthesis (Figure 2B). The two obvious peaks at 13.2 and 28.2° in Figure S5 represented the (100) and (002) crystal planes of C_3N_4, respectively, which were similar to the previous literature.[38] XPS spectra qualitatively reflected the element and bond type information of the prepared materials. For ZnO, two obvious peaks at 1022.2 and 1045.3 eV were ascribed to the $2p_{3/2}$ and $2p_{1/2}$ orbitals of the Zn element (Figure 2C). Figure 2D shows that O 1s in ZnO has two wide peaks at about 530.8 and 532.2 eV, which can be attributed to zinc oxygen bond and impurity oxygen.[39] For BiOI, the peak positions of the Bi element were locked at 158.8 and 164.2ev, corresponding to Bi $4f_{7/2}$ and Bi $4f_{5/2}$ (Figure 2E). The O 1s spectrum was fitted into three characteristic peaks in Figure 2F, which were fixed at 529.7, 531.6, and 533.1 eV, assigning to the bismuth oxygen bond, iodine oxygen bond, and adsorbed oxygen separately. Meanwhile, Figure 2G displays two distinct peaks of I $3d_{5/2}$ and I $3d_{3/2}$ at 618.7 and 630.2 eV, respectively.[40] For C_3N_4, C 1s distinguished three different peaks centered on 284.4, 285.6, and 287.9 eV, which belonged to C−N−C, N−C═N, and C═C bonds, respectively, in turn (Figure 2H). Two peaks located at 397.7 and 399.3 eV were observed in the N 1s spectrum, matching with the C−N═C bond and N−$(C)_3$ group (Figure 2I).[41]

The functional groups and band gap information of materials were obtained through a series of optical characterizations. As shown in Figure S6, the characteristic absorption peaks of different groups on Fourier transform infrared spectroscopy indeed confirmed the amination of ZnO and BiOI and the carboxylation of C_3N_4. The sharp attenuation of absorption intensity at about 400 nm in the UV−vis diffuse reflection spectrum of ZnO reflected that its band gap value was 3.21 eV (Figure S7A).[42] Figure S7B illustrates that the absorption limit of BiOI reached around 600 nm, meaning its

https://doi.org/10.1021/acs.analchem.2c01717
Anal. Chem. 2022, 94, 8075−8084

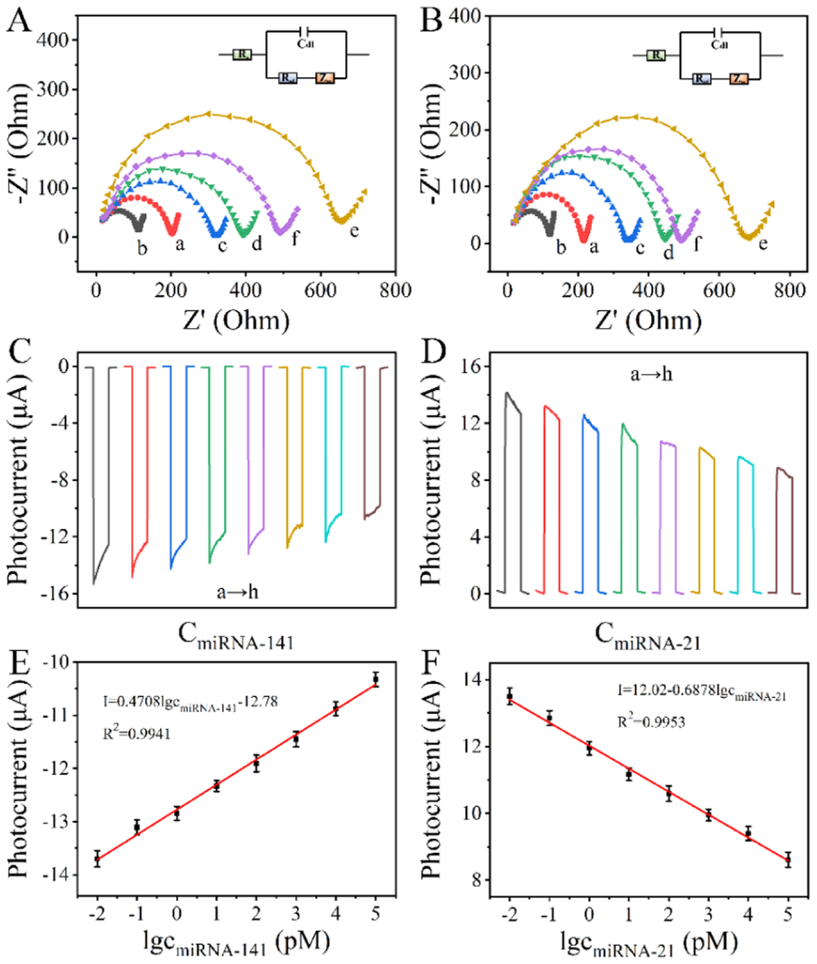

Figure 4. (A) EIS characterization of the miRNA-141 biosensor in 5 mM $[Fe(CN)_6]^{3-/4-}$ solution containing 0.1 M KCl: (a) bare PWE, (b) Au-PWE, (c) BiOI/Au-PWE, (d) C_3N_4-HP/BiOI/Au-PWE, (e) MCH/C_3N_4-HP/BiOI/Au-PWE, and (f) after Cas12a trans-cleavage/MCH/C_3N_4-HP/BiOI/Au-PWE. (B) EIS characterization of the miRNA-21 biosensor under the same conditions: (a) bare PWE, (b) Au-PWE, (c) ZnO/Au-PWE, (d) C_3N_4-HP/ZnO/Au-PWE, (e) MCH/C_3N_4-HP/ZnO/Au-PWE, and (f) after Cas12a trans-cleavage/MCH/C_3N_4-HP/ZnO/Au-PWE. (C) Photocurrent response toward diverse concentrations of miRNA-141 (10 fM, 100 fM, 1 pM, 10 pM, 100 pM, 1 nM, 10 nM, and 100 nM from a to h). (D) Photocurrent response toward miRNA-21 with the same concentration gradient. Linear connection between the photocurrent response and logarithm of concentrations for (E) miRNA-141 and (F) miRNA-21.

efficient visible light utilization ability. On this basis, the band gap of BiOI was calculated to be 1.94 eV, which was consistent with the previous literature.[15] The band gap value (2.71 eV) of C_3N_4 QDs in Figure S7D was obtained according to the boundary of its UV−vis absorption spectrum in Figure S7C.[43] In addition, Figure S7C shows that the emission peak position of C_3N_4 QDs was locked at 555 nm, which was mutually corroborated by its property to emit bright green light under UV lamp irradiation.

Feasibility of the Designed Anode−Cathode Platform. The sensitization of C_3N_4 QDs to BiOI nanospheres or ZnO NSs simultaneously and the feasibility of an anode−cathode cooperative signal amplification strategy were confirmed by the PEC test. As shown in Figure 3B, the original photocurrent response of pure BiOI (curve a) and ZnO (curve c) electrodes was relatively small. Intriguingly, after the size controllable C_3N_4 QDs were immobilized to construct the composite photoelectric layer, the signals of both the C_3N_4/BiOI photocathode (curve b) and C_3N_4/ZnO (curve d) photoanode were significantly improved. When the two photoelectrodes were integrated to build an anode−cathode cooperative PEC platform, the photocurrent response achieved secondary enhancement as expected (Figure 3C).

Figure 3A illustrates the possible mechanism of cascaded amplification of photocurrent signals depended on the calculated energy band, which was attributed to II-scheme (photoanode) and Z-scheme (photocathode) electron transfer mechanisms, respectively.[44,45] For the C_3N_4/ZnO photoanode, both the valence band (VB) and conduction band (CB) of C_3N_4 with a narrow band gap were negative than ZnO, so the photogenerated electrons transitioned to the CB of C_3N_4 were spontaneously injected into the CB of ZnO and immediately transferred to the interface of Au-PWE. Meanwhile, the photogenerated holes on the VB of C_3N_4 were neutralized by the electron donor (ascorbic acid) in the solution, which effectively inhibited the recombination of electron−hole pairs. For the C_3N_4/BiOI photocathode, the CB of BiOI was close to the VB of C_3N_4, resulting in the photogenerated electrons excited to the CB of BiOI tendentiously transfer to the VB of C_3N_4 and finally were captured by the electron acceptor (dissolved oxygen) in the solution. Furthermore, the electrons on the electrode were filled into the photogenerated holes on the VB of BiOI to improve the electron−hole pair separation

https://doi.org/10.1021/acs.analchem.2c01717
Anal. Chem. 2022, 94, 8075−8084

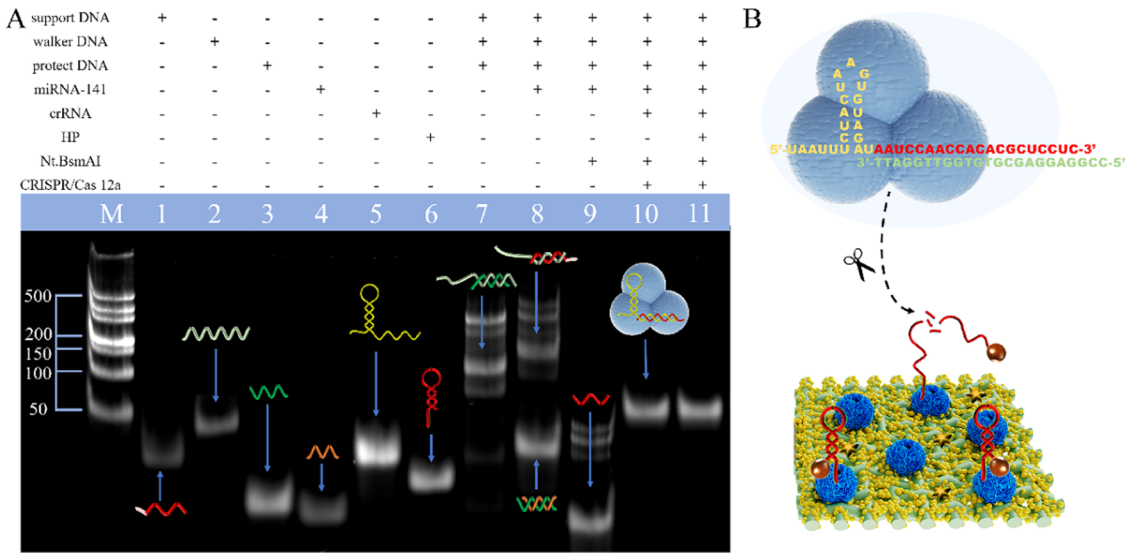

Figure 5. (A) PAGE analysis for the chain displacement mechanism of the 3D DNA nanomachine and trans-cleavage characteristic of CRISPR/Cas12a (M: DNA maker; lane 1: support DNA; lane 2: walker DNA; lane 3: protect DNA; lane 4: miRNA-141; lane 5: crRNA; lane 6: HP; lane 7: support DNA + walker DNA + protect DNA; lane 8: support DNA + walker DNA + protect DNA + miRNA-141; lane 9: support DNA + walker DNA + protect DNA + miRNA-141 + Nt.*Bsm*AI; lane 10: the transformational product T-DNA + crRNA + Cas12a; lane 11: the transformational product T-DNA + crRNA + Cas12a + HP). (B) Schematic diagram of the CRISPR/Cas12a design strategy and trans-cleavage characteristics.

efficiency. Depending on the logical partition of a flexible paper chip, the C_3N_4/ZnO photoanode and C_3N_4/BiOI photocathode were assembled into a circuit. Different from the excitation of a single photoelectrode, the photoanode and photocathode were excited synchronously to produce the photoelectric effect, and their respective abundant photogenerated electrons and photogenerated holes attracted each other, resulting in an ultrafast electron transfer rate.[46] Both electrodes acted as the mutually promoting photoelectric engine to improve the photocurrent response, which also provided sufficient biological reaction areas for dual-target detection.

Construction of the Dual-Target PEC Biosensor. Electrochemical impedance spectroscopy (EIS) was a technique to characterize the changes of electrochemical characteristics on the electrode surface. The difference of charge transfer resistance (R_{et}) was explored by the reversible $[Fe(CN)_6]^{3-/4-}$, which directly reflected the layer-by-layer construction process of the biosensor. Since the modification process of the photoanode and photocathode was similar, the detection of miRNA-141 to gradually modify the photocathode was taken as an example. As shown in Figure 4A, the R_{et} of the unmodified bare paper electrode was relatively small (curve a), while the R_{et} value decreased significantly when conductive Au NPs were grown in situ on the bare electrode (curve b). With the sequential anchoring of BiOI, C_3N_4-HP, and MCH on the Au-PWE surface, the increased steric resistance, electrostatic repulsion, and insulation effect led to the continuous rise of R_{et} (curves c, d, and e). Finally, based on the nonspecific trans-cleavage characteristics of CRISPR/Cas12a, HP was constantly digested, and the C_3N_4 QDs that lost attachment were separated from the electrode surface, resulting in the attenuation of R_{et} (curve f). The experimental results were consistent with expectations, which proved the successful construction of miRNA-141 and miRNA-21 (Figure 4B) dual-target biosensors. In addition, the PEC test was implemented to screen and optimize the influential experimental conditions during the fabrication of biosensors to obtain prominent analytical performance (Figure S8).

The 12% polyacrylamide gel electrophoresis (PAGE) technique was implemented to verify the rationality of the designed 3D DNA nanomachine-mediated CRISPR/Cas12a system. As shown in Figure 5A, support DNA, walker DNA, protect DNA, miRNA-141, crRNA, and HP revealed an obvious single band in lanes 1 to 6 sequentially. The bright band in lane 7 was generated from the swing arm formed by annealing between walker DNA and protect DNA. With the intervention of the target miRNA-141, the original swing arm unwound and the unlocked walker DNA spontaneously paired with support DNA, so that two lightful bands in lane 8 attributed to the miRNA-141/protect DNA and walker DNA/support DNA, respectively. When Nt.*Bsm*AI recognized the active site of walker DNA/support DNA hybrid, lane 9 displayed a prominent characteristic band of transformational product T-DNA in addition to discernible parallel bands. The vivid band in lane 10 represented the formation of Cas12a/crRNA/T-DNA ternary complex, while the addition of HP in lane 11 did not change the number of bands, indicating that the trans-cleavage activity of CRISPR/Cas12a occurred as expected. Moreover, the sequence and cutting process of the programmable CRISPR/Cas12a are demonstrated in Figure 5B.

Detection of MiRNA-141 and MiRNA-21. Under the optimum conditions, parallel PEC characterization with the participation of different concentrations of miRNA-141 and miRNA-21 was performed to evaluate the detection ability of the dual-target biosensor. As shown in Figure 4C,D, the photocurrent intensity was regularly inversely proportional to the concentration of miRNA-141 or miRNA-21 (from 10 fM to 100 nM). The standard curve was drawn by fitting the photocurrent value with the logarithm of miRNA-141 (Figure 4E) or miRNA-21 (Figure 4F) concentration, and the linear regression equations were obtained as follows: $I = 0.4708 \log c_{\text{miRNA-141}} - 12.78$ ($R^2 = 0.9941$) and $I = -0.6878 \log c_{\text{miRNA-21}} + 12.02$ ($R^2 = 0.9953$), in which the detection limits were 5.5

https://doi.org/10.1021/acs.analchem.2c01717
Anal. Chem. 2022, 94, 8075−8084

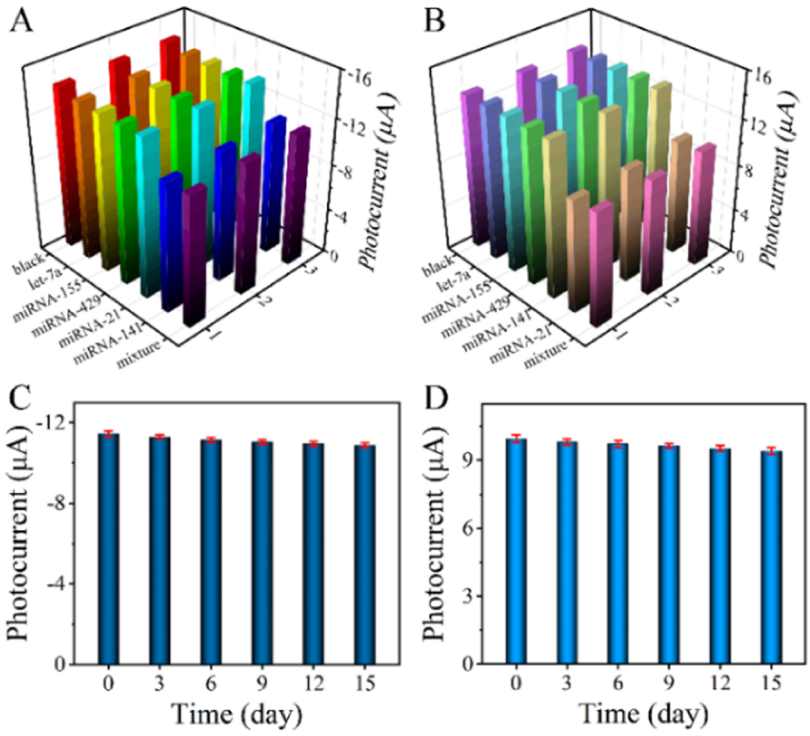

Figure 6. (A) Selectivity of the miRNA-141 biosensor toward the blank, 100 nM let-7a, miRNA-155, miRNA-429, miRNA-21, 1 nM miRNA-141, and miRNAs mixture. (B) Selectivity of the miRNA-21 biosensor toward the blank, 100 nM let-7a, miRNA-155, miRNA-429, miRNA-141, 1 nM miRNA-21, and miRNAs mixture. (C) Stability of the miRNA-141 biosensor (1 nM). (D) Stability of the miRNA-21 biosensor (1 nM).

and 3.4 fM, respectively (S/N = 3). Compared with other works (Table S2), the designed dual-target biosensor possessed certain advantages in monitoring quantity, working range, and detection limit, which owned practical application values.

Analytical Performance and Practical Application of the Dual-Target PEC Biosensor. Highly homologous multiple miRNAs (let-7a, miRNA-155, miRNA-429) were introduced to verify the uniqueness of biosensor response to specific miRNA. As shown in Figure 6A,B, the biosensor was insensitive to interfering miRNAs with a high concentration but strongly responded to target miRNA (miRNA-141 or miRNA-21) with a low concentration. The obvious attenuation of photocurrent proved that the proposed biosensor possessed pre-eminent selectivity. To evaluate the reproducibility of the designed biosensor, five analytical devices fabricated in the parallel batch were tested. As displayed in Figure S9, the intra-assay and interassay RSD of the miRNA-141 biosensor were 2.61 and 3.05%, while the intra-assay and interassay RSD of the miRNA-21 biosensor were 2.82 and 3.48%, respectively, which manifested excellent reproducibility. In addition, a 15-day measurement was conducted to explore whether the sensor component still met the analysis demands after long-term storage at 4 °C. As illustrated in Figure 6C,D, the ultimate photocurrent intensity was maintained at 94.9 and 94.5% of the original value, respectively. The photocurrent changed weakly with storage time, indicating that the prepared biosensor owned prominent stability.

To evaluate the practical application value of the dual-target biosensor, various concentrations of miRNA-141 and miRNA-21 were spiked in real human serum (procured from Shandong Cancer Hospital, China) for the recovery experiment. Tables S3 and S4 show outstanding recovery rates (95.7−106.3% for miRNA-141, while 94.6−105.7% for miRNA-21) and stable RSD values (2.7−4.5% for miRNA-141, while 2.9−4.2% for miRNA-21), which meant that the designed dual-target PEC biosensor effectually inhibited the disturbance of complex coexisting components in biological samples, thus possessing potential for early diagnosis and clinical applications.

CONCLUSIONS

In summary, a dual-engine powered paper PEC platform based on a bipolar cooperative amplification strategy and programmable CRISPR/Cas12a trans-cleavage characteristics was designed. The platform integrated the advantages of materials, equipment, and sensing strategies, which significantly improved the sensitivity and selectivity of analysis. First, the multitype electron transfer mechanism constructed by the interlayer combination of C_3N_4 QDs and ZnO NSs or BiOI nanospheres realized the cascade amplification of photocurrent signals. Second, the independent design and partition of the paper chip functionalized sufficient injection holes and electrode areas, which not only reduced the spatial cross talk to avoid the false-positive problem while monitoring but also endowed the device with rare multitarget detection ability. Finally, the 3D DNA nanomachine owned the capacity of efficient target conversion, and the signal accumulation was driven in synergia with the universal CRISPR/Cas12a system to optimize the analysis performance. Therefore, the proposed PEC biosensor accomplished the ultrasensitive detection of miRNA-141 and miRNA-21, which also provided a pioneering insight and attempt for the construction of other analysis devices.

https://doi.org/10.1021/acs.analchem.2c01717
Anal. Chem. 2022, 94, 8075−8084

■ ASSOCIATED CONTENT

Supporting Information

The Supporting Information is available free of charge at https://pubs.acs.org/doi/10.1021/acs.analchem.2c01717.

Materials and apparatus; synthesis of ZnO NSs; BiOI nanospheres and C_3N_4-HP; false-positive control experiment; fabrication of a paper chip; XRD of C_3N_4; FTIR and UV−vis spectrum of ZnO, BiOI, and C_3N_4; performance of the PEC biosensor and real human serum sample analysis (PDF)

■ AUTHOR INFORMATION

Corresponding Authors

Chao Liu − *Department of Oral and Maxillofacial Surgery, Qilu Hospital of Shandong University; Institute of Stomatology, Shandong University, Jinan 250012, P. R. China;* orcid.org/0000-0002-3971-3919; Email: qiluliuchao@sdu.edu.cn

Shenguang Ge − *Institute for Advanced Interdisciplinary Research, University of Jinan, Jinan 250022, P. R. China;* orcid.org/0000-0002-0537-6491; Email: chm_gesg@163.com

Authors

Chuan Huang − *Institute for Advanced Interdisciplinary Research, University of Jinan, Jinan 250022, P. R. China*

Lu Zhang − *Institute for Advanced Interdisciplinary Research, University of Jinan, Jinan 250022, P. R. China*

Yuanna Zhu − *School of Materials Science and Engineering, University of Jinan, Jinan 250022, P. R. China*

Zuhao Zhang − *Institute for Advanced Interdisciplinary Research, University of Jinan, Jinan 250022, P. R. China*

Yunqing Liu − *Institute for Advanced Interdisciplinary Research, University of Jinan, Jinan 250022, P. R. China*

Jinghua Yu − *School of Chemistry and Chemical Engineering, University of Jinan, Jinan 250022, P. R. China;* orcid.org/0000-0001-5043-0322

Complete contact information is available at: https://pubs.acs.org/10.1021/acs.analchem.2c01717

Author Contributions

⊥C.H. and L.Z. contributed equally to this work.

Notes

The authors declare no competing financial interest.

■ ACKNOWLEDGMENTS

This work was supported by the National Natural Science Foundation of China (22074053, 21874055, and 52172282), the Excellent Youth Innovation Team in Universities of Shandong (2019KJC016), the Project of "20 items of University" of Jinan (2020GXRC047), the Major Scientific and Technological Innovation Project of Shandong Province (2021CXGC010603), and the Taishan Scholars program and Case-by-Case Project for Top Outstanding Talents of Jinan.

■ REFERENCES

(1) Yang, K.; Wang, S.; Cheng, Y.; Tian, Y.; Hou, J. *Oncol. Lett.* **2019**, *17*, 3475−3481.

(2) Bhaskaran, M.; Mohan, M. *Vet. Pathol.* **2014**, *51*, 759−774.

(3) Lu, M.; Zhang, Q.; Deng, M.; Miao, J.; Guo, Y.; Gao, W.; Cui, Q. *PLoS One* **2008**, *3*, No. e3420.

(4) Zhao, W.-W.; Xu, J.; Chen, H. *Chem. Soc. Rev.* **2015**, *44*, 729−741.

(5) Zhao, W.-W.; Xu, J.; Chen, H. *Chem. Rev.* **2014**, *114*, 7421−7441.

(6) Li, H.; Li, J.; Zhu, Y.; Xie, W.; Shao, R.; Yao, X.; Gao, A.; Yin, Y. *Anal. Chem.* **2018**, *90*, 5496−5502.

(7) Wang, J.; Pan, Y.; Jiang, L.; Liu, M.; Liu, F.; Jia, M.; Li, J.; Lai, Y. *ACS Appl. Mater. Interfaces* **2019**, *11*, 37541−37549.

(8) Li, J.; Lin, X.; Zhang, Z.; Tu, W.; Dai, Z. *Biosens. Bioelectron.* **2019**, *126*, 332−338.

(9) Fu, Y.; Zou, K.; Liu, M.; Zhang, X.; Du, C.; Chen, J. *Anal. Chem.* **2020**, *92*, 1189−1196.

(10) Fan, G.-C.; Shi, X.; Zhang, J.; Zhu, J. *Anal. Chem.* **2016**, *88*, 10352−10356.

(11) Wang, G.-L.; Shu, J.; Dong, Y.; Wu, X.; Zhao, W.; Xu, J.; Chen, H. *Anal. Chem.* **2015**, *87*, 2892−2900.

(12) Zang, Y.; Fan, J.; Ju, Y.; Xue, H.; Pang, H. *Chem. − Eur. J.* **2018**, *24*, 14010−14027.

(13) Zhang, X.; Li, W.; Zhou, Y.; Chai, Y.; Yuan, R. *Biosens. Bioelectron.* **2019**, *135*, 8−13.

(14) Yang, H.; Sun, G.; Zhang, L.; Zhang, Y.; Song, X.; Yu, J.; Ge, S. *Sens. Actuators, B* **2016**, *234*, 658−666.

(15) Zhao, C.-Q.; Ding, S.; Xu, J.; Chen, H. *ACS Appl. Nano Mater.* **2020**, *3*, 11489−11496.

(16) Chang, C.; Zhu, L.; Wang, S.; Chu, X.; Yue, L. *ACS Appl. Mater. Interfaces* **2014**, *6*, 5083−5093.

(17) Wang, S.; Wang, F.; Fu, C.; Sun, Y.; Zhao, J.; Li, N.; Liu, Y.; Ge, S.; Yu, J. *Anal. Chem.* **2020**, *92*, 7604−7611.

(18) Li, M.-J.; Zheng, Y.; Liang, W.; Yuan, R.; Chai, Y. *ACS Appl. Mater. Interfaces* **2017**, *9*, 42111−42120.

(19) Yang, T.; Mao, X.; Zhang, Y.; Wu, X.; Wang, L.; Chu, M.; Pao, C. W.; Yang, S.; Xu, Y.; Huang, X. *Nat. Commun.* **2021**, *12*, No. 6022.

(20) Bai, Y.; Zheng, Y.; Wang, Z.; Hong, Q.; Liu, S.; Shen, Y.; Zhang, Y. *New J. Chem.* **2021**, *45*, 11876−11892.

(21) Wang, F.; Liu, Y.; Fu, C.; Li, N.; Du, M.; Zhang, L.; Ge, S.; Yu, J. *Anal. Chem.* **2021**, *93*, 1702−1708.

(22) Huang, C.; Liu, Y.; Sun, Y.; Wang, F.; Ge, S.; Yu, J. *ACS Appl. Mater. Interfaces* **2021**, *13*, 35389−35396.

(23) Feng, J.; Dai, L.; Ren, X.; Ma, H.; Wang, X.; Fan, D.; Wei, Q.; Wu, R. *Anal. Chem.* **2021**, *93*, 7125−7132.

(24) Yang, H.; Xu, M.; Li, Z.; Ge, S.; Zhang, L.; Zhu, P.; Yu, J. *Sens. Actuators, B* **2020**, *316*, No. 128093.

(25) Yang, H.; Wang, J.; Li, X.; Zhang, L.; Yu, H.; Zhang, L.; Ge, S.; Yu, J.; Zhang, Y. *ACS Appl. Mater. Interfaces* **2021**, *13*, 19793−19802.

(26) Li, L.; Zhang, Y.; Yan, Z.; Chen, M.; Zhang, L.; Zhao, P.; Yu, J. *ACS Sens.* **2020**, *5*, 1482−1490.

(27) Peng, H.; Li, X. F.; Zhang, H.; Le, X. C. *Nat. Commun.* **2017**, *8*, No. 14378.

(28) Zhang, P.; Jiang, J.; Yuan, R.; Zhuo, Y.; Chai, Y. *J. Am. Chem. Soc.* **2018**, *140*, 9361−9364.

(29) Peng, R.; Zheng, X.; Lyu, Y.; Xu, L.; Zhang, X.; Ke, G.; Liu, Q.; You, C.; Huan, S.; Tan, W. *J. Am. Chem. Soc.* **2018**, *140*, 9793−9796.

(30) Chen, J. S.; Ma, E.; Harrington, L.; Costa, M.; Tian, X.; Palefsky, J.; Doudna, J. *Science* **2018**, *360*, 436−439.

(31) Zhou, W.; Hu, L.; Ying, L.; Zhao, Z.; Chu, P. K.; Yu, X. F. *Nat. Commun.* **2018**, *9*, No. 5012.

(32) Li, S.-Y.; Cheng, Q.; Liu, J.; Nie, X.; Zhao, G.; Wang, J. *Cell Res.* **2018**, *28*, 491−493.

(33) Xiong, Y.; Zhang, J.; Yang, Z.; Mou, Q.; Ma, Y.; Xiong, Y.; Lu, Y. *J. Am. Chem. Soc.* **2020**, *142*, 207−213.

(34) Zhang, D.; Yan, Y.; Que, H.; Yang, T.; Cheng, X.; Ding, S.; Zhang, X.; Cheng, W. *ACS Sens.* **2020**, *5*, 557−562.

(35) Xu, Z.; Liao, L.; Chai, Y.; Wang, H.; Yuan, R. *Anal. Chem.* **2017**, *89*, 8282−8287.

(36) Han, C.; Chen, Z.; Zhang, N.; Colmenares, J.; Xu, Y. *Adv. Funct. Mater.* **2015**, *25*, 221−229.

(37) Yu, S.-Y.; Mei, L.; Xu, Y.; Xue, T.; Fan, G.; Han, D.; Chen, G.; Zhao, W. *Anal. Chem.* **2019**, *91*, 3800−3804.

(38) Li, C.; Che, H.; Liu, C.; Che, G.; Charpentier, P. A.; Xu, W. Z.; Wang, X.; Liu, L. *J. Taiwan Inst. Chem. Eng.* **2019**, *95*, 669−681.
(39) Zheng, L.; Li, X.; Du, W.; Shi, D.; Ning, W.; Lu, X.; Hou, Z. *Appl. Catal., B* **2017**, *203*, 146−153.
(40) Zhou, X.; Shao, C.; Yang, S.; Li, X.; Guo, X.; Wang, X.; Li, X.; Liu, Y. *ACS Sustainable Chem. Eng.* **2018**, *6*, 2316−2323.
(41) Li, P.; Wang, Y.; Wang, J.; Dong, L.; Zhang, W.; Lu, Z.; Liang, J.; Pan, D.; Fan, Q. *Chem. Eng. J.* **2021**, *414*, No. 128810.
(42) Mahala, C.; Sharma, M.; Basu, M. *New J. Chem.* **2019**, *43*, 7001−7010.
(43) Vu, N.-N.; Kaliaguine, S.; Do, T. *ACS Appl. Energy Mater.* **2020**, *3*, 6422−6433.
(44) He, R.; Cheng, K.; Wei, Z.; Zhang, S.; Xu, D. *Appl. Surf. Sci.* **2019**, *465*, 964−972.
(45) Mahala, C.; Sharma, M.; Basu, M. *ACS Appl. Nano Mater.* **2020**, *3*, 1999−2007.
(46) Xin, X.; He, M.; Han, W.; Jung, J.; Lin, Z. *Angew. Chem., Int. Ed.* **2011**, *50*, 11739−11742.

https://doi.org/10.1021/acs.analchem.2c01717
Anal. Chem. 2022, 94, 8075−8084